



# Structural and Magnetic Characterizations of Ruddlesden–Popper Family ( $\text{Ca}_{2-x}\text{Nd}_x\text{MnO}_4$ ) Compound Synthesized by Ceramic Route

H. Issaoui<sup>1</sup> · F. Issaoui<sup>2</sup> · E. Dhahri<sup>1</sup> · E. K. Hlil<sup>3</sup>

Received: 10 November 2020 / Accepted: 27 January 2021 / Published online: 5 March 2021  
© The Author(s) 2021

## Abstract

In this work, we were interested in the  $\text{Ca}_{2-x}\text{Nd}_x\text{MnO}_4$  compounds when ( $0.1 \leq x \leq 0.4$ ). These oxides are synthesized through the solid-state method. In this study, we investigated the evolution of the structure, the magnetic properties and the  $\text{Mn}^{3+}/\text{Mn}^{4+}$  ratio with the Nd content. The morphological study shows a decrease in the size of the grain in relation to  $x$ . The X-ray diffraction reveals a transition from the tetragonal phase to the orthorhombic phase when  $x=0.4$ . Magnetic measurements have been taken for all the compounds in the temperature range between 2 and 300 K. The temperature-dependent magnetic susceptibility shows the presence of three transitions  $T_N$ ,  $T_C$  and  $T_{CO}$ . A dramatic difference in magnetic susceptibility between ZFC and FC was observed below the Neel temperatures for  $\text{Ca}_{2-x}\text{Nd}_x\text{MnO}_4$ , which shows the onset of a ferromagnetic moment below these temperatures. This moment is caused by the Dzyaloshinskii–Moriya interaction.

**Keywords** Ruddlesden–Popper · Charge ordering · Anisotropy

## 1 Introduction

The interest in materials with a perovskite structure is explained by their potential technological applications arising from their various and interesting physical properties [1–3]. The Mn-based perovskite oxides have been a renewed subject of numerous investigations in recent years [4–7] because of their colossal magnetoresistance and giant volume magnetostriction near room temperature, which is required by

---

✉ F. Issaoui  
issawi\_fatma@yahoo.fr

<sup>1</sup> Laboratoire de Physique Appliquée, Faculté Des Sciences de Sfax, B.P 1171, Sfax 3000, Tunisie

<sup>2</sup> Research Unit Valorization and Optimization of Resource Exploitation, Faculty of Science and Technology of Sidi Bouzid, University of Kairouan, 9100 Sidibouzid, Tunisia

<sup>3</sup> Institut Néel, CNRS–Université J. Fourier, BP166, 38042 Grenoble, France

the technology of various sensors and magnetomechanical devices. The  $\text{Ca}_2\text{MnO}_4$  also has a layered perovskite structure. However, it does not have an ideal Ruddlesden–Popper-type structure, i.e., the octahedra  $\text{MnO}_6$  of the compound rotate slightly around the  $c$  axis from an ideal Ruddlesden–Popper-type structure with the space group  $I4/mmm$ . As a result, it takes a tetragonal unit cell with the space group  $I41/acd$ , and its unit cell is related to the  $\text{K}_2\text{NiF}_4$ -type unit cell in the following way:  $a = \sqrt{2}a'$  and  $c = 2c'$  (where  $a'$  and  $c'$  are the lattice parameters for the  $\text{K}_2\text{NiF}_4$ -type unit cell) [8].  $\text{Ca}_2\text{MnO}_4$  shows an unusual magnetic susceptibility behavior, with a very shallow maximum around 220 K and a fairly sharp peak at 114 K [9, 10]. A powder neutron diffraction study of this compound has revealed that three-dimensional ordering sets in at 114 K with an antiferromagnetic structure different from that of  $\text{K}_2\text{NiF}_4$  [9].

The layered perovskite manganite  $\text{Ca}_2\text{MnO}_4$  containing only  $\text{Mn}^{4+}$  ions has the  $\text{K}_2\text{NiF}_4$ -type of structure [11]. The doping of divalent ions by the trivalent ions, which made a change in the structural and magnetic properties of the first one and the structure of solid solutions of  $\text{Ca}_{2-x}\text{Ln}_x\text{MnO}_4$  ( $\text{Ln} = \text{Pr}, \text{Nd}, \text{Sm}, \text{Eu}$  and  $\text{Gd}$ ) at room temperature, was first investigated by Daoudi and Le Flem [12] and Chaumont et al. [13]. In this family, there are two kinds of crystal structure: One is the tetragonal phase and the other is the orthorhombic phase. The former appears in Pr at  $X=0$  [3], and also for Y, but on the other hand this transition varies according to the element of substitution: For example, for Sm, this transition is reported at  $x=0.3$  [14]. The latter has axes of  $a_0$  and  $b_0$  which are related to the tetragonal axis of  $a_T$  by  $a_0 \approx b_0 \approx \sqrt{2} a_T$ . Otherwise, this substitution leads to a ferromagnetic double-exchange interaction between  $\text{Mn}^{3+}$  and  $\text{Mn}^{4+}$  that results from the motion of an  $e_g$  electron between the two partially filled  $d$  shells with a strong on-site Hund's coupling [15, 16].

In this mechanism, the kinetic energy of the  $e_g$  electrons increases at the cost of an enhancement of an antiferromagnetic coupling via the  $t_{2g}$  electrons. Recent studies have shown that these exchange mechanisms cannot, by themselves, explain the observed behavior in these systems and suggested that the canted moments [17], the spin structures [18], the magnetic clusters [19], the strong electron–phonon interaction arising from the lattice distortion associated with the Jahn–Teller splitting of the Mn  $e_g$  level [20] and the spin glass [21] play a crucial role in changing the number of  $\text{Mn}^{3+}$  and  $\text{Mn}^{4+}$  ions in the samples.

The purpose of this work is to report on the effect of the substitution of the trivalent  $\text{Nd}^{3+}$  ion for the divalent  $\text{Ca}^{2+}$  ion on the crystallographic and magnetic properties of the  $\text{Ca}_{2-x}\text{Nd}_x\text{MnO}_4$  ( $0.1 \leq x \leq 0.4$ ) compounds. It also aims to determine the anisotropy constants of the studied compounds.

## 2 Experimental Techniques

### 2.1 Synthesis

The  $\text{Ca}_{2-x}\text{Nd}_x\text{MnO}_4$  samples were prepared by means of a solid-state reaction method [22]. The precursors of  $\text{CaO}$ ,  $\text{Nd}_2\text{O}_3$  and  $\text{MnO}_2$  (all of 99% purity) were

mixed in appropriate ratios. The obtained powders were pressed under 4 tones into pellets about 1 mm in thickness and 8 mm in diameter and calcined at 1100 °C for 4 days in air with several intermediate regrinding and repressing into pellet. Finally the mixtures were sintered in the air at 1523 K for 24 h.

## 2.2 Apparatus

The phase purity, homogeneity and lattice structure of the synthesized compound were obtained by X-ray diffraction (XRD) analysis, using an X-ray powder diffractometer (Siemens D5000) with  $\text{CuK}\alpha$  radiations ( $\lambda = 1.54056 \text{ \AA}$ ).

Microstructures and grain sizes were observed by means of a scanning electron microscope (SEM). The pictures were taken at room temperature on a Philips XL 30 equipped with a field emission gun at 19.7 kV.

The magnetization measurements were taken using a vibrating sample magnetometer in the temperature range 5–300 K with an applied field up to 0.05 T. A domain study at low temperature was performed using the protocol ZFC/FC, which is an experimental procedure that allows to take measurements of magnetization as a function of the temperature  $M$  (T) under the action of a weak magnetic field of about 500 Oe (FC) or without magnetic field (ZFC). The range of temperature explored extends from 5 to 300 K. These measurements were taken using an extraction magnetometer ( $\text{BS}_2$ ).

## 3 Results and Discussion

### 3.1 Structural Properties

#### 3.1.1 X-ray Diffraction

The X-ray diffraction (XRD) profiles (see Fig. 1) were indexed with a tetragonal structure ( $I4/mmm$  space group) for  $x \leq 0.3$  and an orthorhombic one ( $\text{Pnma}$  space group) for  $x = 0.4$ . Such behavior is in agreement with Takahaski's results [23]. This transition type is also observed with other rare earth doping such as Pr [24], Nd and Y [25].

In order to confirm the structure of materials, Goldschmidt's tolerance factor  $t_G$  as an indicator for the stability and distortion of crystal structure was calculated [26]:

$$t_G = \frac{r_A + r_O}{(r_B + r_O)\sqrt{2}}$$

where  $r_A$ ,  $r_B$  and  $r_O$  are the radii of A, B and O site ions in the  $\text{ABO}_4$  structure, respectively.

The arithmetic values of the ionic rays of ions occupying sites A, B and O, respectively.

Are calculated as follows:

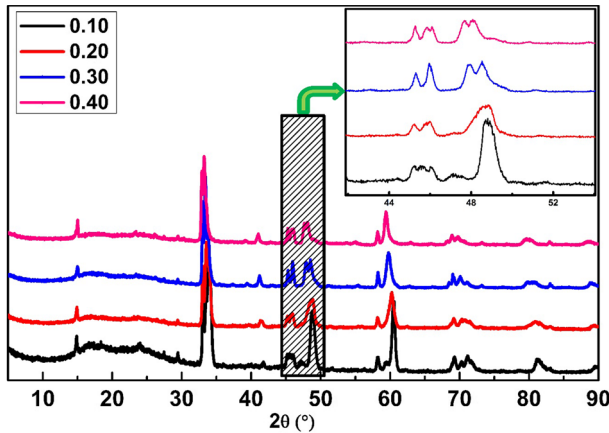


Fig. 1 X-ray diffraction data for polycrystalline CNMO (Color figure online)

$$\langle r_O \rangle = r_{O^{2-}}$$

$$\langle r_B \rangle = r_{Mn^{3+}}$$

$$\langle r_A \rangle = (2 - x)r_{Ca^{2+}} + xr_{Nd^{3+}}$$

The calculated tolerance factor values are given in Table 1. According to this table, it can be seen that the  $t_G$  values decrease with the increase in the Nd rate due to a decrease in the average ionic radius of the site A. The decrease in the tolerance factor  $t_G$  brings about the system to the most symmetrical structure.

In order to determine the average crystallite size, we have used the Scherer method [27]; below is a detailed explanation of this method of calculation.

$$D_{SC} = \frac{0.9 \times \lambda}{\beta \times \cos\theta} \tag{1}$$

where ( $\lambda = 1.541 \text{ \AA}$ ) is the wave length of the CuK  $\alpha$  radiation,  $\theta$  is the diffraction angle for the most intense peak (2 0 0) and  $\beta$  is defined as:

$$\beta^2 = \beta_m^2 - \beta_s^2 \tag{2}$$

Table 1 Mean ion radii ( $\langle r_A \rangle$ ) and tolerance factors

$x$	0.10	0.20	0.30	0.40
Space group	I/4mmm	I/4mmm	I/4mmm	Pnma
$\langle r_A \rangle (\text{\AA})$	2.358	2.356	2.354	2.353
Tolerance factors (t)	1.2994	1.0376	1.0369	1.0366

Here,  $\beta_m$  is the experimental full width at half maximum (FWHM) of a standard silicon sample [28].

The mean values of the crystallite size, summarized in Table 2, confirm that all compounds are of nanometer size.

## 4 Morphological Study

### 4.1 Scanning electron microscope (SEM)

The morphology and the size of the particles for the compounds  $0.1 \leq x \leq 0.4$  are observed with the SEM photograph (inset Fig. 2). The obtained micrographs show that the samples are constituted of homogenous particles. Histograms displayed in Fig. 2 shows that the particles are distributed according to a Lorentzian function. Particle size distribution can significantly affect the magnetic properties of samples [29]. Table 2 presents the values obtained from the grain size, determined using ImageJ software.

Obviously, the particle sizes observed by SEM are several times larger than those calculated by XRD, which indicates that each particle observed by SEM consists of several crystallized grains.

## 5 Magnetic Study

Figure 3 shows the variation of the magnetization as a function of the temperature for all compositions which were measured under an applied magnetic field of 0.05 T. All samples undergo a PM–FM transition upon lowering of the temperature. On the other hand, the variation of  $dM/dT$  shows that there are three transitions: The first two are defined from the minimum of the first derivative of the magnetization as a function of the temperature denoted, respectively, as  $T_N$  and  $T_C$ . The third is the  $T_{CO}$  charge control temperature (defined from the maximum of the first derivative of the magnetization as a function of temperature) which occurs at high temperature. The  $T_N$ ,  $T_C$  and  $T_{CO}$  values for the samples ( $0.1 \leq x \leq 0.4$ ) are given in Table 3. Note that the substitution has no effect for  $x=0.1$  and  $x=0.2$  on the transition temperatures, on the other hand it increases progressively for  $x=0.3$  and 0.4: The compound  $Ca_2MnO_4$  contains only the  $Mn^{4+}$  ions which are responsible for the antiferromagnetic interaction by the super-exchange interaction via 2p orbitals of oxygen. The substitution of trivalent  $Nd^{3+}$  ions for divalent  $Ca^{2+}$  ions led to the appearance of  $Mn^{3+}$  ions. Therefore, the coexistence of  $Mn^{3+}$  and  $Mn^{4+}$  ions promotes a ferromagnetic coupling by the super-exchange interaction, via oxygen 2p orbitals. As the Nd replaces the Ca sites, this causes a gain in the

**Table 2** Grain size

x	0.1	0.2	0.3	0.4
DG(nm)	57.968	57.782	56.900	56.711
DC(nm)	5.465	5.237	4.753	4.342

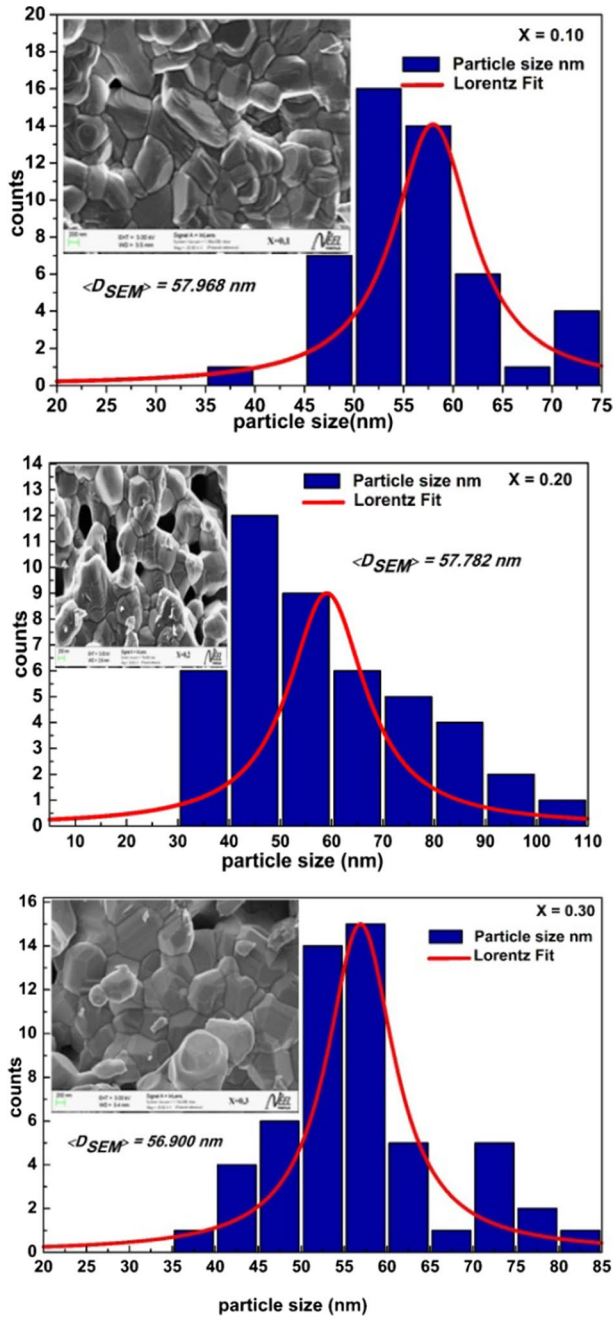


Fig. 2 Typical scanning electron micrographs (SEM) of CNMO samples (Color figure online)

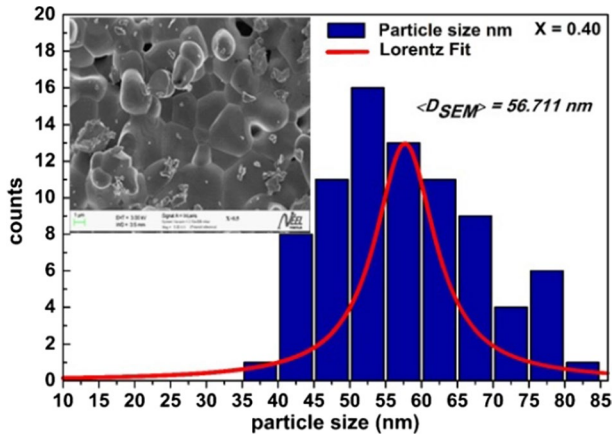


Fig. 2 (continued)

$\text{Mn}^{3+}/\text{Mn}^{4+}$  ratio. The population of electrons hopping and the number of available jump sites increase. Therefore, the double-exchange becomes important, thus implying the growth of ferromagnetism as the Nd content increases [30]. To better explain the origin of ferromagnetism, according to the double-exchange interaction introduced by Zener in 1951 [16], an electron of the 2p orbital of oxygen was delocalized on the level of  $e_g$  ( $\text{Mn}^{4+}$ ) and the orbital, thus evacuated, was filled by an electron from the level of  $e_g$  ( $\text{Mn}^{3+}$ ) with conservation of the spin orientation (Rule of Hund). Finally, in our compound we have a competition between a weak antiferromagnetic interaction and the ferromagnetic interaction, which necessitates a ZFC/FC study.

Figure 4 illustrates the low-temperature magnetic behavior of  $\text{Ca}_{2-x}\text{Nd}_x\text{MnO}_4$  in the temperature range 2 K–300 K. The zero-field-cooled (ZFC) and field-cooled (FC) data are measured by a  $\text{BS}_2$  magnetometer. The sample was first cooled to 2 K, and then, the ZFC and FC magnetizations were measured during heating without a magnetic field and applying a field of 500 Oe, respectively, with intermediate cooling. Both the ZFC and FC variations are characteristic of a complex magnetic behavior with maximum values goes from 0.74  $\mu\text{em/g}$  to 0.165  $\mu\text{em/g}$  in the ZFC curve.

The temperature-dependent irreversibility magnetization for all the compounds is shown in Fig. 5. For all compounds, the divergence between the ZFC and FC magnetization increases with the decrease in temperature, as also can be seen from  $M$ - $T$  plots. The percentage change in irreversibility magnetization, i.e., the bifurcation between ZFC and FC is 40% in  $x=0.1$ , is significantly high in comparison with 6%  $x=0.2$  and 0.3. This large divergence generally depicts the presence of competing FM and AFM interactions and the presence of magnetic anisotropy in the compound [31, 32]. A small peak in the vicinity of Neel temperature ( $\sim 110$  K) of CNMO also corresponds to the AFM behavior of the compound.

In set Fig. 5, the variation of the ZFC curve shows that when the temperature is decreased, a maximum followed by a drastic reduction is produced. This behavior is observed for all compounds. This maximum corresponds to the temperature of

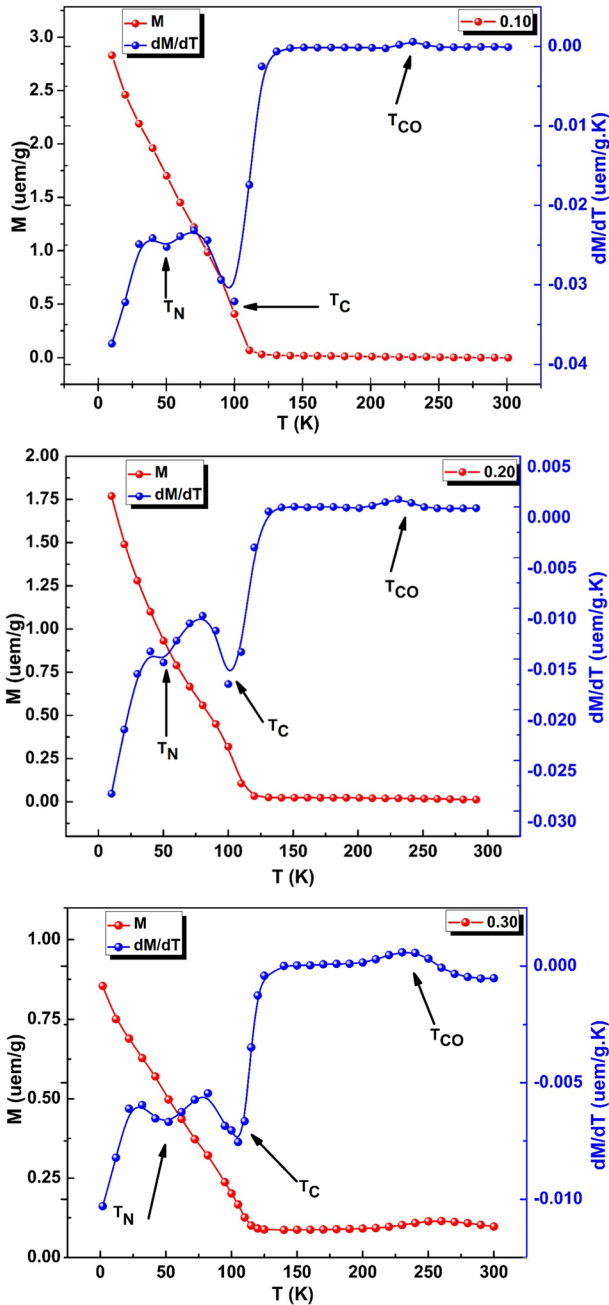


**Fig. 3** Magnetization variation as a function temperature for CNMO and derivative of magnetization as a function of temperature (Color figure online)



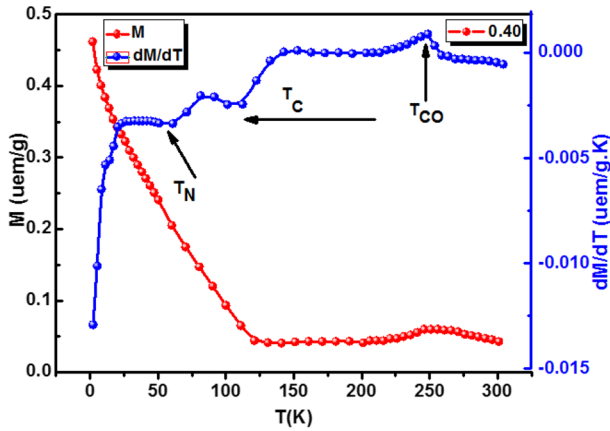


Fig. 3 (continued)

**Table 3** Values of the transitions temperatures for different concentrations (x)

x	T <sub>N</sub>	T <sub>C</sub>	T <sub>CO</sub>
0.1	50	100	231
0.2	50	100	231
0.3	52	105	240
0.4	60	111	246

spin glass T<sub>SG</sub>, which decreases as x increases. This moment can be related to the spin glass state enhanced by the Dzyaloshinskii–Moriya interaction [33] (Fig. 6).

For T lower than T<sub>B</sub>, a phenomenon of super-paramagnetic relaxation is observed due to the reduced size of the grains. The super-paramagnetic relaxation time is given by this formula:

$$\tau = \tau_0 \exp\left(-\frac{E_a}{k_B T}\right) \tag{3}$$

where E<sub>a</sub> is the energy barrier separating the energy minima, T is the temperature, τ<sub>0</sub> ~ 10<sup>-12</sup> – 10<sup>-9</sup>s and k<sub>B</sub> is the Boltzmann constant [34].

The critical size for a particle is super-paramagnetic and is defined by considering the magnetization switches once per second, which corresponds to [35]:

$$E_a = KV = 25k_B T \tag{4}$$

The particles are assumed to be spherical. The volume (V) of a particle is of the order of d<sub>s</sub><sup>3</sup>, where d<sub>s</sub> is the diameter of a particle and it is related to the anisotropy constant by:

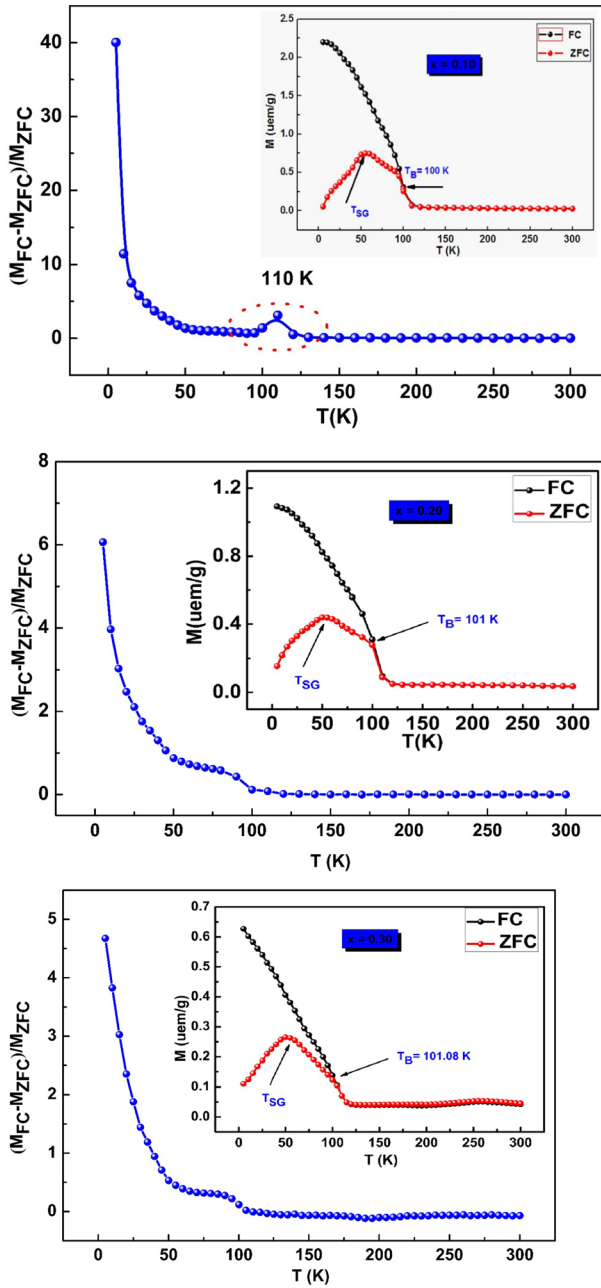


Fig. 4 Irreversibility magnetization vs temperature for CNMO (Color figure online)

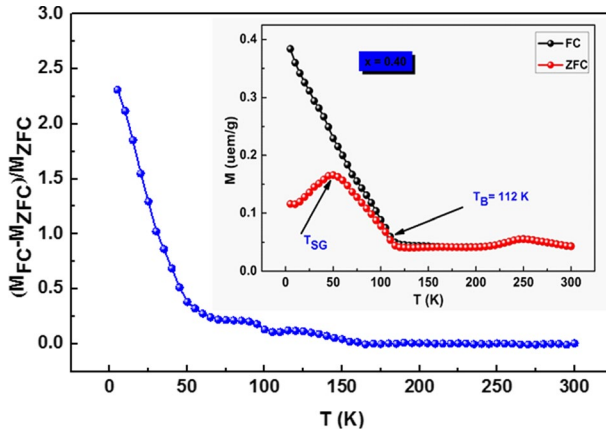


Fig. 4 (continued)

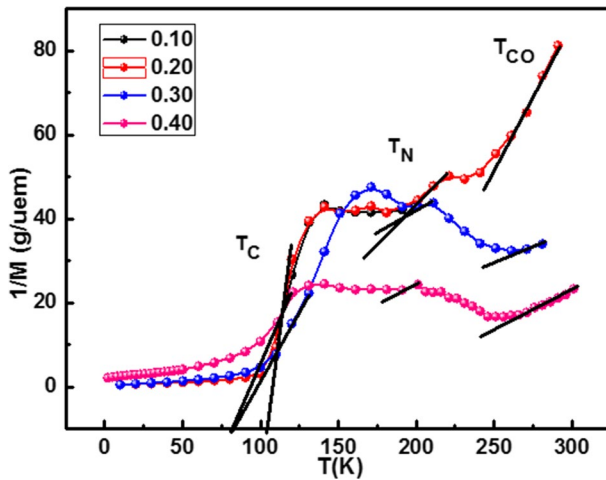
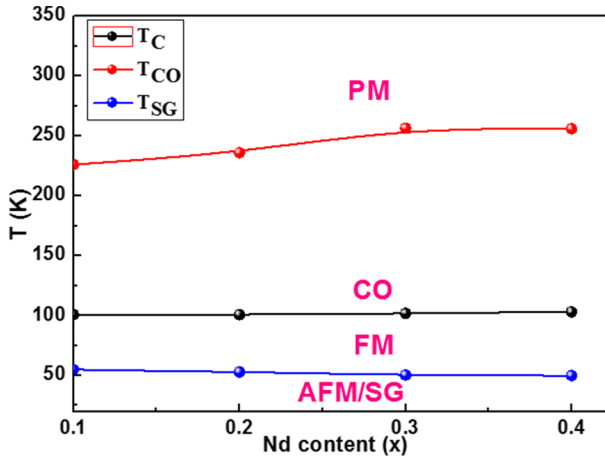


Fig. 5 Temperature dependence of the reciprocal magnetization ( $1/M$ ) of CNMO measured under  $H=0.05$  T T. The solid lines are fits to the Curie–Weiss law (Color figure online)

$$d_s \approx \left( \frac{25k_B T}{K} \right)^{1/3} \tag{5}$$

Table 3 shows that the blocking temperature and the anisotropy energy increase with the rate of substitution of neodymium. Finally, the anisotropy constant is calculated using the values of  $d_s$  calculated by means of the Scherrer method. Since the anisotropy constants are positive, we will have three easy magnetization directions which are the three crystallographic directions similar to the case of Fe (centered cubic structure) [36].



**Fig. 6** Phase diagram of CNMO with  $0 < x < 0.4$ , where PM, CO, FM and AF represent the paramagnetic phase, charge ordering phase, ferromagnetic phase and antiferromagnetic phase, respectively (Color figure online)

The susceptibility presents the Curie–Weiss-type behavior  $\chi = C/T - \theta_{CW}$  for the temperatures little above 55 K. Here,  $C$  and  $\theta_{CW}$  are Curie constant and Curie–Weiss temperature, respectively.

The value of  $\theta_{CW}$  is negative (see Fig. 4), indicating that the local magnetization maximum is associated with the antiferromagnetic AF–ferromagnetic FM transition.

With the increase in the Sr content, this signature of AF ordering shifts slightly to low temperature and appears as a subtle shoulder. In this case, Neel temperature (TN) can be defined as the temperature corresponding to the minimum of  $dM/dT$  around that shoulder. At high temperatures, the  $M$ – $T$  curve exhibits a distinct maximum at a certain temperature ( $T_{CO}$ ).

At high temperatures, the  $M$ – $T$  curve exhibits a distinct maximum at a certain temperature ( $T_{CO}$ ). With the introduction of a Sr ion,  $T_{CO}$  increases almost linearly. It is 231 K for  $x=0.1$  and 246 K for  $x=0.4$ , which means that 2% Nd causes a increase in  $T_{CO}$  by about 9 K. For the temperatures between  $T_{CO}$  and  $T_N$ , the susceptibilities of all the compounds show Curie–Weiss-type behaviors with a positive  $\theta_{CW}$  value, signaling a local ferromagnetic correlation. The theoretical effective moment is calculated through the equation:

$$\mu_{eff}^{the} = g\sqrt{J(J+1)} \quad (6)$$

where  $g = 1 + \frac{J(J+1)+S(S+1)-L(L+1)}{2J(J+1)}$  Landé factor,  $J = |S + L|$  total moment,  $L = \sum m_l$  orbital moment and  $S = \sum m_s$  spin moment.

The theoretical value of the magnetic moments is too low compared to that observed experimentally. In order to obtain magnetic moments which are close to those of the experiment, one can imagine the formation of polarons containing four manganese cations (4Mn) which are coupled ferromagnetically, and the value of the magnetic moment associated to the polarons is given by the following formula:

**Table 4** Temperature blocking energy anisotropy, anisotropy constant, the Curie constant, the Curie–Weiss temperature, the theoretical and experimentally value of the magnetic moments, for compound  $\text{Ca}_{2-x}\text{Nd}_x\text{MnO}_4$ 

Composition	$\text{Ca}_{1.9}\text{Nd}_{0.1}\text{MnO}_4$	$\text{Ca}_{1.8}\text{Nd}_{0.2}\text{MnO}_4$	$\text{Ca}_{1.7}\text{Nd}_{0.3}\text{MnO}_4$	$\text{Ca}_{1.6}\text{Nd}_{0.4}\text{MnO}_4$
$T_B$ (K)	100.0100	105.0400	108.6500	112.7000
$E_a$ (mev)	215.6600	226.4900	234.2700	243.1800
$\lambda$ (mol/emu)	2.3200	2.3200	1.2790	1.1400
$C$ (emu.K/mol)	2.5961	2.3674	1.9900	0.7256
$\theta_{WC}$ (K)	99.0200	99.8800	101.7100	72.6000
$\mu_{eff}^{exp}(\mu_B)$	1.7550	1.8380	2.0040	3.3204
$\mu_{eff}^{th}(\mu_B)$	4.1440	4.4017	4.4800	4.8758

$$\mu_{eff}(4Mn) = \sqrt{\mu_{eff}^2(4Mn)} \quad (7)$$

These results are given in Table 4. The difference between  $T_C$  and  $\theta_{WC}$  could be better explained by the appearance of a magnetic inhomogeneity which may be due to the formation of polarons between Zener manganese cations, e.g., sharing two electrons suggests the formation of magnetic clusters above  $T_C$ .

Knowledge of the paramagnetic Curie temperature  $\theta_{WC}$  provides access to the molecular field constant  $\lambda$  which is defined as the ratio of the molecular field to the magnetization  $M$ . This molecular field is related to the Curie constant by  $\lambda = \theta_{WC} / C$ , where  $C$  denotes the Curie–Weiss constant (Table 3).

Based on the above studies, a phase diagram of CNMO system is presented in Fig. 6. It demonstrates the evolution of magnetic structure with the content of Nd. According to the previous reports, by the doping of Nd, ferromagnetic microregions can be produced in the matrix of CO phase due to an AF spin coupling between  $\text{Nd}^{3+}$  and  $\text{Mn}^{4+}$ . Besides, the doping of trivalent ions also introduces the B-site randomness and causes the deviation of  $\text{Mn}^{4+}/\text{Mn}^{3+}$  ratio from 1:1, which is disadvantageous to the coherence of the CO phase [36–40]. Thus, these two factors are the main reasons for the depression of CO phase. On the other hand, the smaller  $\text{Nd}^{3+}$  ion in the  $\text{Mn}^{3+}\text{-O-Mn}^{4+}$  bond not only changes  $\text{Mn}^{3+}/\text{Mn}^{4+}$  ratio, but also causes the neighboring  $\text{Mn-O}$  bond length and  $\text{Mn}^{3+}\text{-O-Mn}^{4+}$  angle to deviate from the undoped case, then leads to lattice distortions. These lattice distortions may disfavor the FM interaction between Mn ions. The competition between FM ordering and AF ordering presumably determines the variation of  $T_N$ . For the case of low Nd content, the FM ordering could be weak and its effects may be canceled out by those associated with the lattice distortion.

## 6 Conclusion

In this work, we studied the role of the doping effect in the structural and magnetic properties of  $\text{Ca}_{2-x}\text{Nd}_x\text{MnO}_4$  oxides. Doping  $x$  produces a structural and magnetic phase transition. We found that when  $x$  increases, for  $x < 0.3$ , we have a tetragonal structure and for  $x > 0.3$  an orthorhombic system. The magnetic measurement shows that the Curie temperature  $T_C$  increases with an increasing concentration of Nd doping. In addition, magnetization decreases when  $x$  is increased. This effect can be explained by a big ferromagnetic double-exchange interaction between the ions of  $\text{Mn}^{4+}$  and  $\text{Mn}^{3+}$ .

**Acknowledgements** Funding was provided by FSTSBZ.

**Open Access** This article is licensed under a Creative Commons Attribution 4.0 International License, which permits use, sharing, adaptation, distribution and reproduction in any medium or format, as long as you give appropriate credit to the original author(s) and the source, provide a link to the Creative Commons licence, and indicate if changes were made. The images or other third party material in this article are included in the article's Creative Commons licence, unless indicated otherwise in a credit line to the material. If material is not included in the article's Creative Commons licence and your intended use is not permitted by statutory regulation or exceeds the permitted use, you will need to obtain permission directly from the copyright holder. To view a copy of this licence, visit <http://creativecommons.org/licenses/by/4.0/>.

## References

1. K. Barner, H. Deng, W. Morsakov, I.V. Medvedev, C.P. Yang, *J. Alloys Compd.* **500**, 16–21 (2010)
2. H. Yi Liu, C. Kong, *J. Alloys Compd.* **439**, 33–36 (2007)
3. M.T. Tlili, M. Bejar, E. Dhahri, M. Sajjeddine, M.A. Valente, E.K. Hlil, *J. Mater. Charact.* **62**, 243–247 (2011)
4. A. Tozri, E. Dhahri, E.K. Hlil, *J. Magn. Magn. Mater.* **322**, 2516–2524 (2010)
5. Y. Feng, M. Zhang, *J. Magn. Magn. Mater.* **322**, 2675–2679 (2010)
6. P.T. Phong, N.V. Dai, D.H. Manh, T.D. Thanh, N.V. Khiem, L.V. Hong, N.X. Phuc, *J. Magn. Magn. Mater.* **322**, 2737–2741 (2010)
7. S.K. Misra, S.I. Andronenko, S. Asthana, D. Bahadur, *J. Magn. Magn. Mater.* **322**, 2902–2907 (2010)
8. K. Poeppelmeier, M.E. Leonwicz, J.M. Longo, *J. Solid State Chem.* **59**, 71 (1985)
9. D.E. Cox, G. Shirane, R.J. Birgeneau, J.B. MacChesney, *Phys. Rev.* **188**, 930 (1969)
10. J.B. MacChesney, H.J. Williams, J.F. Potter, R.C. Sherwood, *Phys. Rev.* **164**, 779 (1967)
11. C. Chaumont, A. Daoudi, G. Le Flem, P. Hagenmuller, Préparation, propriétés cristallographiques, magnétiques et électriques de la solution solide  $\text{Ca}_{2-x}\text{Y}_x\text{MnO}_4$ , *J. Solid State Chem.* **14**, 335–341 (1975)
12. A. Daoudi, G. Le Flem, *J. Solid State Chem.* **5**, 57 (1972)
13. C. Chaumont, A. Daoudi, G. Le Flem, P. Hagenmuller, *J. Solid State Chem.* **14**, 335 (1975)
14. J. Takahashi, T. Kikuchi, H. Satoh, N. Kamegashira, *J. Alloys Compds.* **192**, 96 (1993)
15. C. Zener, *Phys. Rev.* **82**, 403 (1951)
16. M.T. Tlili, N. Chihaoui, M. Bejar, E. Dhahri, M.A. Valente, E.K. Hlil, *J. Alloys Compd.* **509**, 6447–6451 (2011)
17. A. Urushibara, Y. Moritomo, T. Arima, A. Asamitsu, G. Kido, Y. Tokura, *Phys. Rev. B* **51**, 14103 (1995)
18. J. Inoue, S. Maekawa, *Phys. Rev. Lett.* **74**, 3407 (1995)
19. J.Z. Sun, L. Krusin-Elbaum, A. Gupta, G. Xiao, S.S.P. Parkin, *Appl. Phys. Lett.* **69**, 1002 (1996)
20. A.J. Millis, B.I. Shraiman, R. Mueller, *Phys. Rev. Lett.* **77**, 175 (1996)

21. J.M. De Teresa, M.R. Ibarra, J. Garcia, J. Blasco, C. Ritter, P.A. Algarabel, C. Marquina, A. Del Moral, *Phys. Rev. Lett.* **76**, 3392 (1996)
22. N. Sdiri, M. Bejar, M. Hussein, S. Mazen, E. Dhahri, *J. Magn. Magn. Mater.* **316**, e703–e706 (2007)
23. W. Bao, J.D. Axe, C.H. Chen, S.W. Chenong, *Phys. Rev. Lett.* **78**, 543 (1997)
24. H. Woo, T.A. Tyson, M. Croft, S.W. Cheong, J.C. Woicik, *Phys. Rev. B* **63**, 134412 (2001)
25. F. Issaoui, M. Bejar, E. Dhahri, M. Bekri, P. Lachkar, E. K. Hlil, *Physica* (2013) B414; 42–49.
26. V.M. Goldschmidt, *Geochemistry* (Oxford University Press, Oxford, 1958).
27. Z.Q. Li, E.Y. Jiang, S.W. Ren, D.L. Hou, P. Wu, H.L. Bai, *Phys. Status Solidi A* **195**(2), 429–433 (2003)
28. A. Guinier, in: X. Dunod (Ed.), *theorie et Technique de la radiocristallographie*,
29. A.C. Gandhi, P.M. Reddy, T.S. Chan, Y.P. Ho, S.Y (2015) *5*, 84782
30. N. Kamegashira, A. Shimonono, H.W. XU, H. Satoh, K. Hayashi and T. Kikuchi (1990) *Matchem and phys.* **26**; 483–492.
31. C. Autret, R. Retoux, M. Hervieu, B. Raveau, *Chem. Mater.* **13**, 4745 (2001)
32. L. Daniel (2003) *Modélisation multi-échelle du comportement magnéto-mécanique des matériaux ferromagnétiques texturés*, thèse de doctorat, école Normale Supérieure de Cachan
33. Keitaro Tezuka, Masaaki Inamura, and Yukio Hinatsu (1999) *Journal of Solid State Chemistry.* (145, 705); 710
34. Q. Feng, K. Yanagisawa, N. Yamasaki, Hydrothermal soft chemical process for synthesis of manganese oxides with tunnel structures. *J. Porous Mater.* **5**, 153–161 (1998)
35. E. I. Turkevich and V. P. Plakhitii, *Fiz. Tverd. Tela ~Leningrad* (1968) **10**; 951
36. J. Sin, T.H. Tidfel, M. McCormack, R.A. Fastnachit, R. Ramesh, L.H. Chen, *Science* **264**, 413 (1994)
37. Y. Tomioka, A. Asamitsu, H. Kuwara, Y. Moritomo, and Y. Tokura, *Phys. Rev. B* **53**, R1689 ~1996!
38. Y. Moritomo, H. Kuwahara, Y. Tomioka, Y. Tokura, *Phys. Rev. B* **55**, 7549 (1997)
39. A. Machida, Y. Moritomo, K. Ohoyam, T. Katsufuji, A. Nakamura, *Phys. Rev. B* **65**, 064435 (2002)
40. Y. Moritomo, A. Machida, S. Mori, N. Yamamoto, A. Nakamura, *Phys. Rev. B* **60**, 9220 (1999)

**Publisher's Note** Springer Nature remains neutral with regard to jurisdictional claims in published maps and institutional affiliations.